Supporting Information

Cascade Nanozymatic Network Mimicking Cells with Selective and Linear Perception of H_2O_2

Caixia Zhu,[a] Zhixin Zhou,[a] Xuejiao J. Gao,[b] Yanhong Tao,[b] Xuwen Cao,[a] Yuan Xu,[a] Yanfei Shen,[a] Songqin Liu,[a] Yuanjian Zhang[a]*

[a]Jiangsu Engineering Laboratory of Smart Carbon-Rich Materials and Device, Jiangsu Province Hi-Tech Key Laboratory for Bio-Medical Research, State Key Laboratory of Bioelectronics, School of Chemistry and Chemical Engineering, Medical School, Southeast University, Nanjing 21189, China. Email: Yuanjian.Zhang@seu.edu.cn
[b]College of Chemistry and Chemical Engineering, Jiangxi Normal University, Nanchang, 330022, China

Contents

Experiments

Chemicals. Sodium dodecyl sulfate (SDS) was purchased from Energy Chemical. Cobalt (II) chloride hexahydrate ($CoCl_2 \cdot 6H_2O$), ethanol, hydrogen peroxide (H_2O_2, 30%), acetic acid (HAc), sodium acetate trihydrate ($NaAc \cdot 3H_2O$), and dimethyl sulfoxide (DMSO) were purchased from Sinopharm Chemical Reagent Co., Ltd. (China). 1-butyl-3-methylimidazolium bromide, TMB, sodium dodecyl benzene sulfonate (SDBS), cetyltrimethylammonium bromide (CTAB), Tween 20, and ascorbic acid (AA) were purchased from Aladdin Chemistry Co., Ltd. (China). Dicyandiamide (DCDA, 99%), and peroxidase (HRP, from horseradish, >250 units/mg) were purchased from Sigma-Aldrich (USA). Unless otherwise specified, all other chemicals were of analytical grade and used without further purification. Ultrapure water (18.2 MΩ cm) was obtained from a Direct-Q 3 UV pure water purification system (Millipore, USA).

Characterization. The morphology of Co-N-CNTs was characterized by using scanning electron microscopy (SEM) on a FEI Inspect F50 (FEI, USA). The transmission electron microscopy (TEM) and high-resolution transmission electron microscopy (TEM) images were obtained from a Tecnai G2 F30 (FEI, USA) at an accelerating voltage of 300 kV. Aberration-corrected scanning transmission electron microscopy (STEM) images were investigated by Themis Z (FEI, USA) at 200 kV equipped with a Gatan Enfina electron energy loss spectrometer. X-Ray diffraction (XRD) patterns were performed on an Ultima IV (Rigaku, Japan). The absorbance of the samples was measured by a Cary 100 UV-vis (Agilent, Singapore). The generated oxygen was measured by an oxygen electrode on JPSJ-605 (Leici, China). The pH value of solutions was measured by pH meter (PHS-3C, Leici, China).

Oxidase-like activity of Co-N-CNTs nanozyme. TMB (50 mM, 10 μL) and Co-N-CNTs (5 mg/mL, 10 μL) were mixed in 1 mL of 0.1 M HAc-NaAc buffer solution (pH 3.5, the optimal pH obtained by experiments) with incubation for 3 min in a 1.5 mL centrifuge tube. Then the absorbance of the blue product at 652 nm was recorded via UV-vis spectroscopy. For the response of H_2O_2, identical conditions except that the buffer solution contained various concentrations of H_2O_2 (0.1 mM, 1 mM, 10 mM, and 100 mM) were used.

To obtain the steady-state kinetic parameters of Co-N-CNTs, the reaction was carried out in a HAc-NaAc buffer solution (pH 3.5) with TMB (10, 20, 40, 50, 60, 80, 100, 150

and 200 mM) as reaction substrates. The activity of Co-N-CNTs for catalyzing the oxidation of TMB was assessed by monitoring the time dependent absorbance (at 652 nm for the TMB_{ox1}) change via the kinetic mode using a Cary 100 UV-vis spectrometer (Agilent, Singapore). According to the Lambert-Beer law, the concentration change rate of TMB_{ox1} was calculated based on the following formula (1) and (2):

$$C = \frac{A}{\varepsilon l} \quad (1)$$

$$V = \frac{C}{t} = \frac{\Delta A/\Delta t}{\varepsilon l} \quad (2)$$

where A is the absorbance of TMB_{ox1} at 652 nm, C is the concentration of TMB_{ox1} that is calculated by the Lambert-Beer law, V is initial reaction velocity, $\Delta A/\Delta t$ is the initial rate of change in absorbance at 652 nm s^{-1}, ε is the molar absorption coefficient of TMB ($\varepsilon_{652\ nm}$ = 39,000 $M^{-1}\ cm^{-1}$), and l is the path length of light traveling in the cuvette (l = 0.1 cm).

The kinetics constants V_{max} and K_M were calculated by fitting the reaction velocity values and the substrate concentrations to the Michaelis-Menten equation (3) as follows:

$$V = \frac{V_{max} \times [S]}{K_M + [S]} \quad (3)$$

where V_{max} is the maximal reaction rate that is observed at saturated substrate concentration, [S] is the concentration of the substrate and K_M is the Michaelis constant.

The catalytic constant (k_{cat}) were calculated using the following equation (4)[1]:

$$k_{cat} = \frac{V_{max}}{[E]} \quad (4)$$

where k_{cat} is the rate constant defining the maximum number of substrate molecules converted to product per unit of time. [E] is the nanozyme concentration (M).

Catalase-like activity of Co-N-CNTs nanozyme. H_2O_2 (10 M, 50 μL) and Co-N-CNTs (5 mg/mL, 50 μL) were mixed in 5 mL of 0.1 M HAc-NaAc buffer solution (pH 3.5) with stirring at room temperature and the dissolved oxygen concentration (mg/L) was recorded at different time. The influence of TMB addition on the catalase-like activity of Co-N-CNTs was carried out under identical conditions, except that the reaction solution contained TMB (50 mM, 50 μL).

Calculation Details. The generalized gradient approximation with the Perdew–Burke–

Ernzerhof functional with vdW corrections estimated in the DFT-D3BJ form[2-4] was used for all geometry optimizations and energy calculations. An energy cut-off of 500 eV and Gaussian smearing of 0.05 eV were utilized. The Hubbard *U* correction with *U* defined as U_{eff} was set as 3.42 for Co to treat the strong on-site Coulomb interaction of the localized *d* electrons.[5] For all calculations, the (3 × 3 × 1) Monkhorst−Pack meshes were used for the k-point samplings[6]. The convergence thresholds for the electronic structure and forces were set to be 10^{-5} eV and 0.02 eV $Å^{-1}$, respectively. All calculations were performed using the VASP package with projector-augmented wave pseudopotential.[7-9]

Cascade reaction. Firstly, the substrate TMB_{ox1} was prepared by oxidation of TMB. Briefly, 6 mL of acetate buffers solution (0.1 M, pH 3.5) of TMB (0.5 mM) and Co-N-CNTs catalyst (0.05 mg/mL) were mixed in a reaction vessel. The oxidation was carried out under the air-saturated condition for about 15 min. After filtration, Co-N-CNTs in the solution were removed. The absorption of TMB_{ox1} (652 nm) was measured by UV-vis absorption spectra and the concentration of TMB_{ox1} was determined using the Lambert-Beer law. Then, this solution was divided into equal parts and different concentrations of SDS (0 - 20 mM) were added into each solution. After incubation for 3 min, the absorption of TMB_{ox1} (652 nm) and TMB (285 nm) was measured by UV-vis absorption.

Reaction in microfluidic devices. Co-N-CNTs were immobilized on the poly(dimethylsiloxane) (PDMS) wall of the first chamber and sealed with glass slide. The reaction in the microfluidic device was conducted in identical conditions to the aforementioned procedures. The product of all the following experiments was collected three times in succession.

Cascade reaction in microfluidic devices. As shown in Figure 4a, the HAc/NaAc solution (0.1 M, pH 3.5) containing TMB (0.5 mM) was pumped (10 μL/min) into the microfluidic chamber from the Entrance 1. Meanwhile, Entrance 2 remained closed. When the TMB solution flowed into the first reaction chamber, TMB oxidation reaction occurred on Co-N-CNTs, resulting in TMB_{ox1}. To realize the cascade reaction, the SDS micelle (10 mM) was pumped (10 μL/min) from Entrance 3. After reaction in the second chamber (without Co-N-CNTs), the reactive solution was spilled from the outlet and collected. The absorption of TMB_{ox2} (450 nm) and TMB_{ox1} (652 nm) was detected

through UV-vis absorption spectra (Figure 5b).

H_2O_2 response in microfluidics as cell mimics.

Linear response to H_2O_2 under feedback mode. As shown in Figure S12a, the HAc/NaAc solution (0.1 M, pH 3.5) containing TMB (0.5 mM) was pumped (10 μL/min) into the first chamber from Entrance 1. Meanwhile, the HAc/NaAc solution (0.1 M, pH 3.5) containing different concentrations of H_2O_2 was pumped (10 μL/min) into the first chamber from Entrance 2 and mixed with the TMB solution at the crossing point. During this experiment, Entrance 3 remained closed. When the mixed solution flowed into the first reaction chamber, the oxidation of TMB with different degrees occurred on Co-N-CNTs (about 0.4 mg/chamber). The reactive solution was spilled from the outlet and collected. The absorption of TMB_{ox1} was detected through UV-vis absorption spectra (Figure S12b).

Linear response to H_2O_2 response under feedforward mode. As shown in Figure S12c, the HAc/NaAc solution (0.1 M, pH 3.5) containing TMB (0.5 mM) was pumped (10 μL/min) into the microfluidic chamber from the Entrance 1. Meanwhile, Entrance 2 remained closed. When the TMB solution flowed into the first reaction chamber, TMB oxidation reaction occurred on Co-N-CNTs, resulting in TMB_{ox1}. Then, SDS micelle (10 mM) with different concentration H_2O_2 was pumped (10 μL/min) from Entrance 3. After reaction in the second chamber (without Co-N-CNTs), the reactive solution was spilled from the outlet and collected. The absorption of TMB_{ox2} (450 nm) and TMB_{ox1} (652 nm) was detected through UV-vis absorption spectra (Figure S12d).

Synthesis

Synthesis of Co-N-CNTs. Co-N-CNTs were prepared by a high-temperature pyrolysis, followed by using a chemical vapor deposition-like method (Figure S1). First of all, 1-butyl-3-methylimidazolium bromide (10.96 g) and $CoCl_2 \cdot 6H_2O$ (11.89 g) were first stirred together in anhydrous ethanol (120 mL) at RT for 10.5 h. The product was distilled to remove ethanol solvent in a rotary evaporator and washed with an ample amount of anhydrous ether. After drying at 80 °C overnight under vacuum, Co-N-C precursor ($[BMIM]CoBrCl_3$) was obtained. Secondly, to get Co-N-C, the precursor (1 g) was pyrolyzed at 800 °C in N_2 with a ramp rate of 10 °C/min. Finally, the Co-N-C powder (105 mg) was heat-treated again with DCDA (1.51 g) at 750 °C in N_2 atmosphere. The product was leached in concentrated hydrochloric acid (25 mL) at RT for 9 h and washed with an ample amount of deionized (DI) water. The final product (Co-N-CNTs, 156 mg) was obtained by drying at 80 °C in a vacuum oven overnight.

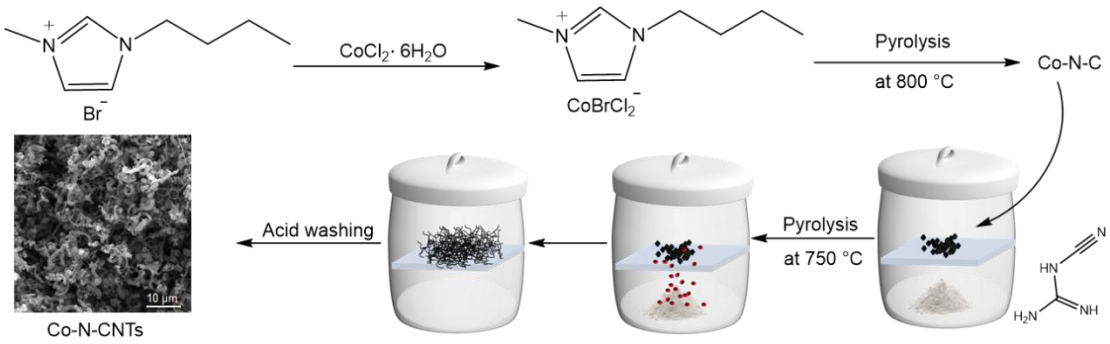

Figure S1. General procedures for synthesizing Co-N-CNTs.

Characterization and properties of Co-N-CNTs

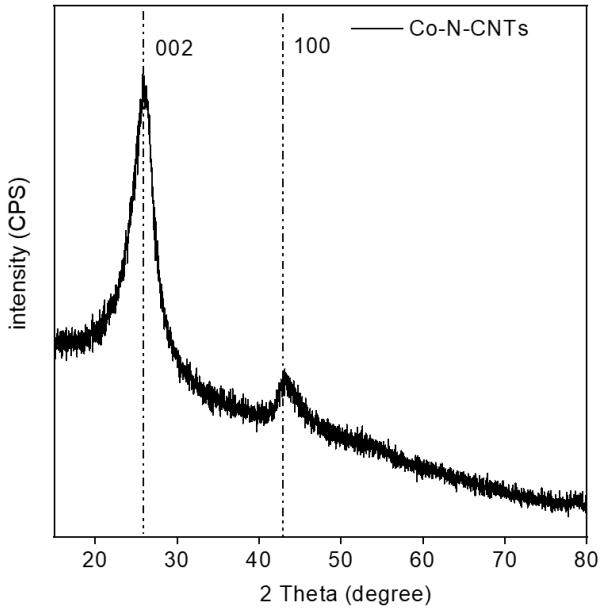

Figure S2. X-ray powder diffraction pattern of Co-N-CNTs.

In the XRD pattern, there were two peaks at about 26 and 44 degrees, which correspond to the (002) and (100) crystal planes of graphite structure, respectively, indicating the generation of graphitization structure in Co-N-CNTs.

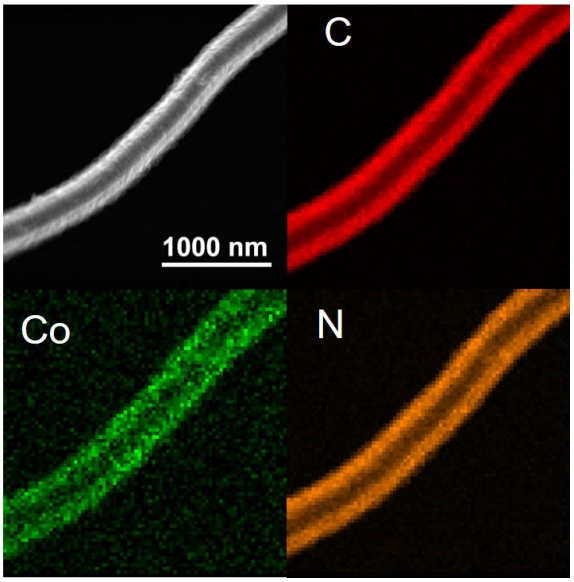

Figure S3. SEM image and the corresponding element mapping images of Co-N-CNTs**.**

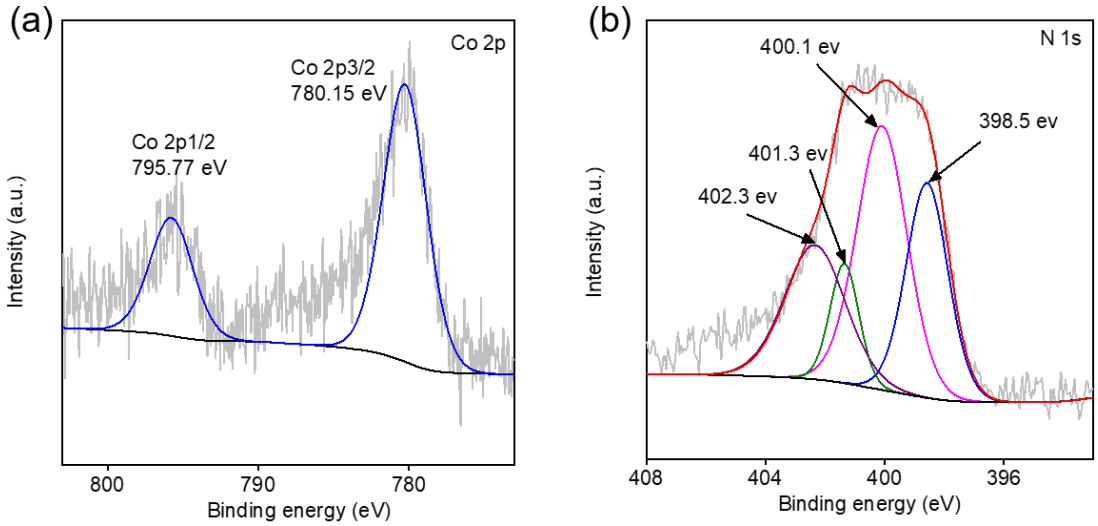

Figure S4. High-resolution Co 2p (a) and N 1s (b) XPS spectra.

To reveal the electronic structure of Co-N-CNTs, X-ray photoelectron spectroscopy (XPS) was performed. The high-resolution Co 2p XPS spectrum (Figure S4a) showed two peaks at a binding energy of 780.3 and 796.7 eV, corresponding to the $2p_{3/2}$ and $2p_{1/2}$ levels, respectively. The binding energy of Co $2p_{3/2}$ was higher than that of Co^0 (778.8 eV) and Co^{3+} (779.6 eV), but lower than that of Co^{2+} (781.1 eV),[10-11] suggesting the valence state of Co was between +2 and +3. The high-resolution N 1s spectrum of Co-N-CNTs (Figure S4b) can be deconvoluted into four peaks, assigned to pyridinic- (398.5 eV), pyrrolic- (400.1 eV), graphitic- (401.3 eV), and oxidized- (402.3 eV) N species.[12-13] The quantitative calculation revealed that the atomic ratios of N in Co-N-CNTs (3.16 at%) were higher than that in the Co-N-C precursor catalyst (0.99 at%).

Table S1. Best-fitted EXAFS results of different samples.[a]

Sample	Shell	CN	R (Å)	σ^2 ($Å^2$)	ΔE_0 (eV)	R-factor
Co foil	Co-Co	12	2.5	0.006	6.6	0.001
CoPc	Co-N	4	1.89	0.002	2.3	0.03
Co-N-CNTs	Co-N	4	1.86	0.008	-11.5	0.04

[a]CN is the coordination number for the absorber-back scatterer pair, R is the average absorberback scatterer distance, σ^2 is the Debye-Waller factor, and ΔE_0 is the inner potential correction. R-factor is goodness of fit.

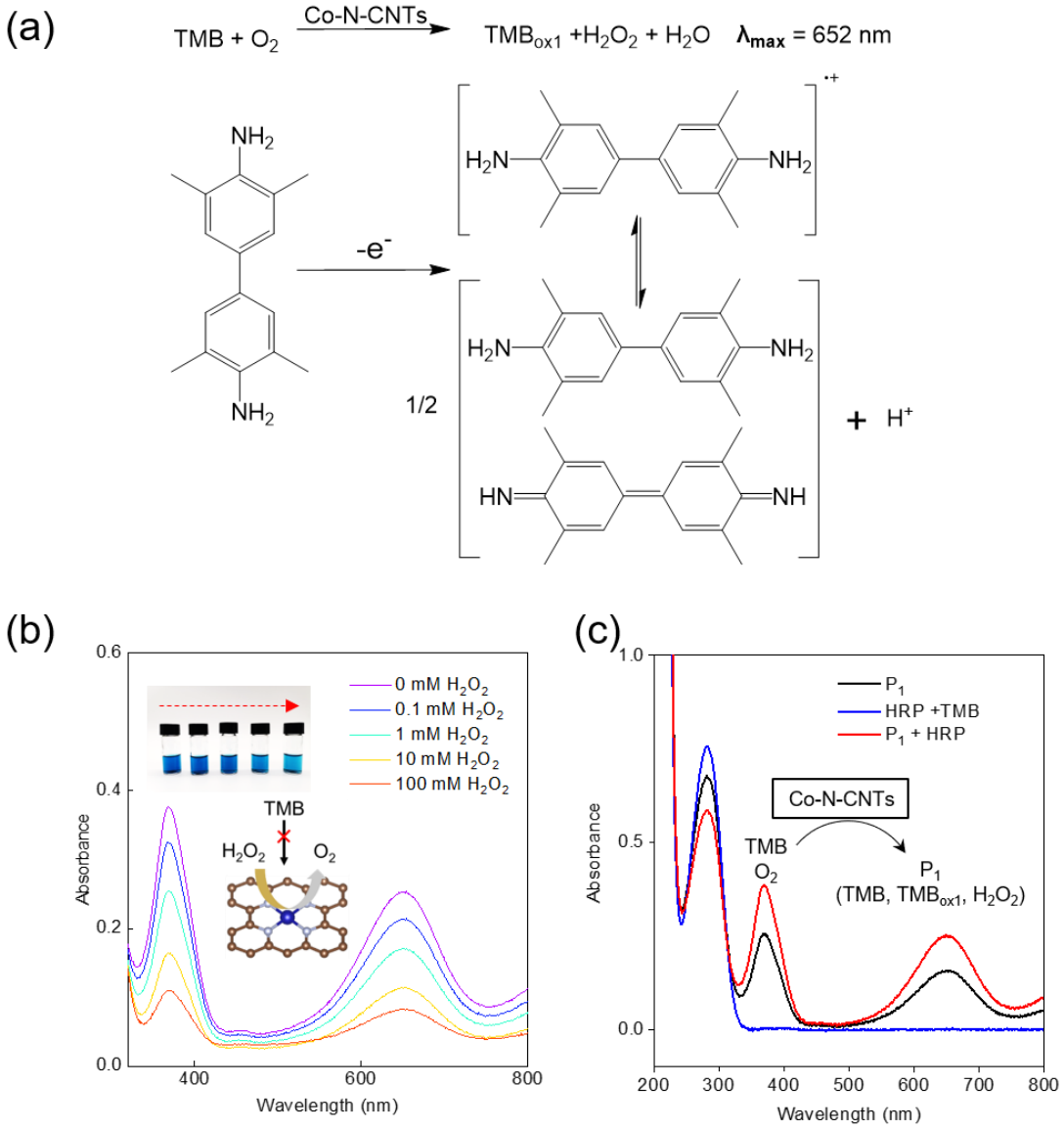

Figure S5. (a) Reaction scheme of oxidation of TMB.[14] (b) UV-vis absorption spectra of TMB catalyzed by Co-N-CNTs in presence of different concentrations of H_2O_2. (c) UV-vis spectra of P_1 solution after incubation with or without HRP (0.01 mg/mL) (P_1 refers to the product solution of TMB oxidation by Co-N-CNTs).

As shown in Figure S5b, the absorbance intensity at 652 nm (TMB_{ox}) was found to be inversely proportional to the concentration of H_2O_2 by chromogenic assay. This confirmed that the addition of H_2O_2 was not favorable to the color development reaction of TMB oxidation catalyzed by Co-N-CNTs. It indicated that the competition rather than co-catalysis occurred between the substrate H_2O_2 and O_2 (TMB).

The reduction products of O_2 were studied by TMB-HRP chromatography. The oxidation reaction of TMB was performed in acetate buffer solution containing 0.05

mg/ml Co-N-CNTs. The oxidation tests were undertaken under an air-saturated condition and incubated for 10 min. After filtration, Co-N-CNTs of the reaction solution were removed (the supernatant going to be reactant solution referred to as P_1). The UV-vis plot of P_1 was shown in Figure S5c. The oxidation of TMB catalyzed by Co-N-CNTs nanozyme was known to have the following two possibilities:

$$O_2 + 4TMB \rightarrow 2H_2O + 4TMB_{ox1} \quad (1)$$

$$O_2 + 2TMB \rightarrow H_2O_2 + 2TMB_{ox1} \quad (2)$$

The TMB_{ox1} of the solution P_1 were calculated by using the Lambert–Beer law:

$$C = \frac{A}{\varepsilon l}$$

Where A is the absorbance of TMB_{ox1} at 652 nm, C is the concentration of TMB_{ox1} that is calculated by the Lambert–Beer law, ε is the molar absorption coefficient of TMB ($\varepsilon_{652\ nm}$ = 39,000 $M^{-1}\ cm^{-1}$), and l is the path length of light traveling in the cuvette (l = 0.1 cm). After the calculation, the sum of TMB_{ox1} concentrations produced by Equations 1 and 2 was 0.04 mM

Next, the amount of H_2O_2 was determined by adding HRP to the P_1 solution and the reaction equation is as follows:

$$H_2O_2 + 2TMB \rightarrow 2H_2O + 2TMB_{ox1} \quad (3)$$

HRP (10 μL, 2 mg/ml) was added into the obtained P_1 solution. After the reaction was complete, the absorbance of solution was tested by UV-vis spectrometer. As shown in Figure S5c, the UV-vis plot of the reaction solution P_1 with the addition of HRP showed a significant increase in the absorption peak at 652 nm compared to the control sample, indicating that H_2O_2 was generated during the catalytic oxidation of TMB by Co-N-CNTs with O_2. The concentration of TMB_{ox1} catalyzed by HRP (H_2O_2) was 0.02 mM calculated from the difference with P_1. The stoichiometric ratio of H_2O_2 and TMB_{ox1} was 1:2 according to Equations 3. Therefore, the concentration of H_2O_2 was 0.01 mM. Similarly, combining the above information, it can be obtained that the reaction amount of TMB in Equations 1 and 2 is 0.02 mM. The results showed that the possibility of oxygen reduction through four-electron or two-electron pathways was equal during the oxidation activity of Co-N-CNTs.

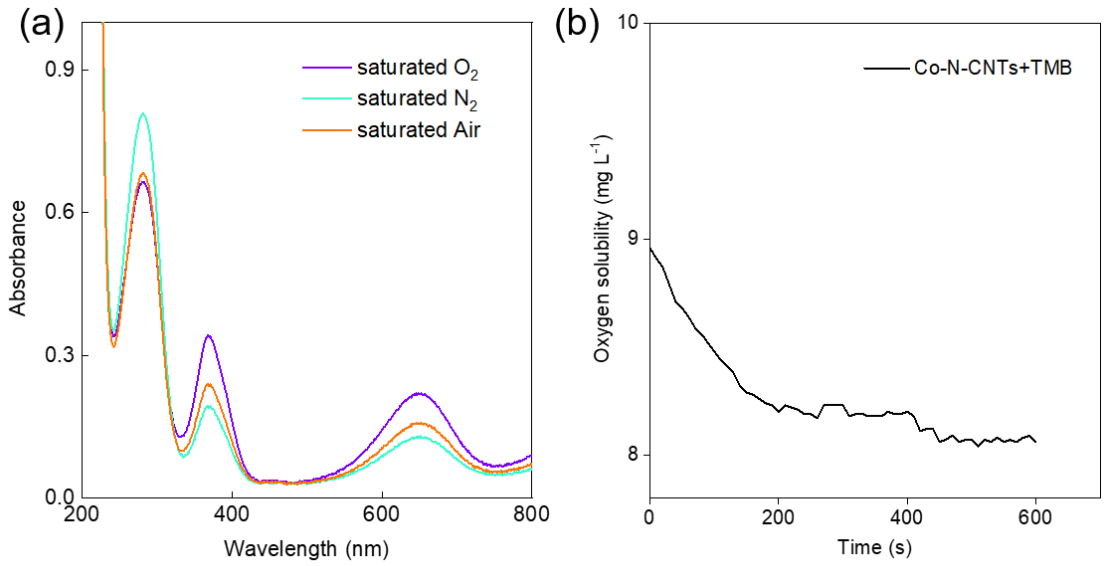

Figure S6. Role of O_2 in the catalytic oxidation of TMB by Co-N-CNTs. (a) UV-vis spectra of Co-N-CNTs-TMB system in O_2, air, and N_2 saturated solutions. (b) The dissolved oxygen concentration of solution on the oxidation of TMB (0.5 mM) catalyzed by Co-N-CNTs.

To probe the role of O_2 in the catalytic oxidation of TMB by Co-N-CNTs, the control experiments were conducted in O_2, air, and N_2 saturated solutions. A distinct difference value was observed at 652 nm in the UV-vis absorption (Figure S6a), verifying that O_2 played a role in the oxidation of TMB. As shown in Figure S6b, the dissolved oxygen concentration was significantly decreased with the catalysis of Co-N-CNTs, verifying that O_2 takes part in this reaction to oxidize TMB.

Table S2. Comparison of Michaelis-Menton constants (K_M) and maximum reaction rates (V_{max}) of reported oxidase-like nanozymes.

Nanozymes	K_M (mM)	V_{max} ($\mu M \cdot s^{-1}$)	Ref.
Fe-N-C-400	0.27	0.34	[15]
Fe-N-C-850	0.23	0.13	[15]
Pd_{12} nanocage	0.24	0.07	[16]
Fe-N-C SAzymes	1.81	0.601×10^{-3}	[17]
FeCoZn-TAC/SNC	0.459	0.223	[18]
Co-N-CNTs	0.15	0.25	This work

Table S3. Comparison of Michaelis-Menton constants (K_M) and maximum reaction rates (V_{max}) of reported catalase-like nanozymes.

Nanozymes	K_M (mM)	V_{max} ($mM \cdot s^{-1}$)	Ref.
Fe-SANzyme	18.80	9.32×10^{-3}	[19]
Catalase	52.14	1.27×10^{-2}	[19]
Pt-Ft	420.60	0.84	[20]
Au-Si-ACD	117.00	1.18×10^{-4}	[21]
CN	393.30	2.48×10^{-3}	[22]
Co-N-CNTs	11.00	1.31	This work

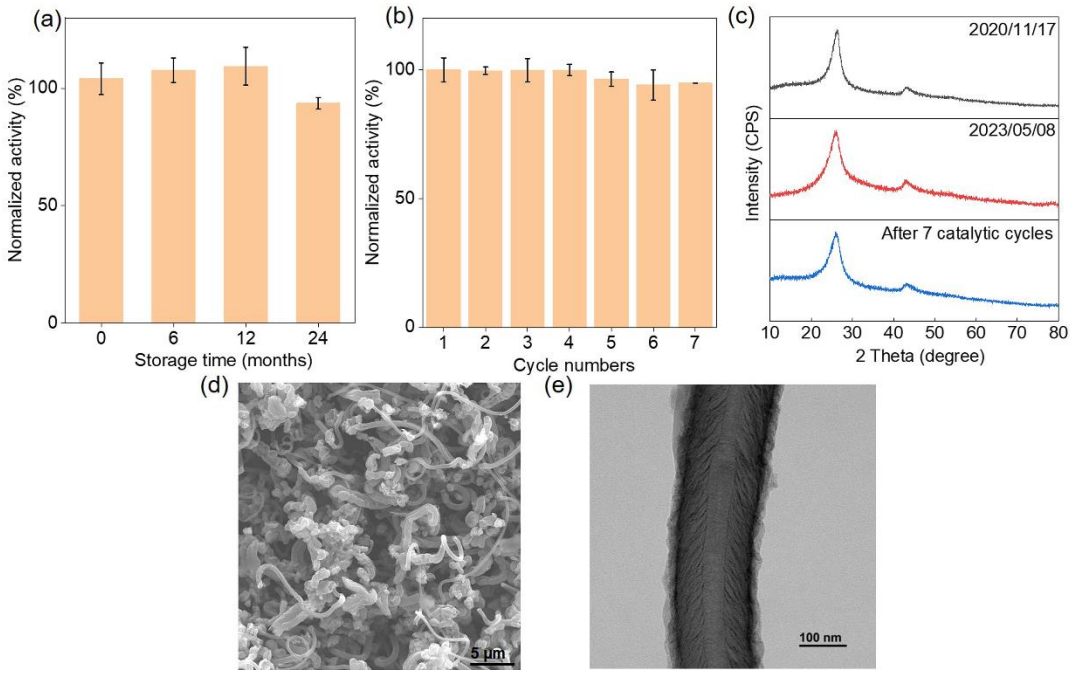

Figure S7. Stability study of the catalyst. Catalytic activity of the Co-N-CNTs nanozymes relative to (a) storage time and (b) cycle numbers. (c) X-ray powder diffraction patterns of the original Co-N-CNTs (top), after long-term storage (middle)and after seven catalytic cycles (bottom). SEM (d) and TEM (e) images of Co-N-CNTs after the catalytic oxidation of TMB and H_2O_2.

To evaluate the stability of the Co-N-CNTs nanozymes, the long-term stability and reusability were investigated. The Co-N-CNTs nanozyme was kept at room temperature and the catalytic activity was measured over one year period to investigate the long-term stability (Figure S7a). The Co-N-CNTs nanozyme exhibited only a slight decrease in catalytic activity after two years, thus indicating that the Co-N-CNTs nanozyme was easy to store and show excellent long-term stability. As can be seen in Figure S7c (middle), the powder X-ray diffraction (XRD) patterns also showed that the graphite structure of Co-N-CNTs after long-term storage did not change significantly compared with the initial catalyst. In addition, the Co-N-CNTs nanozyme was collected by centrifugation after each reaction, washed twice with water, and redispersed into water for reuse. The oxidase-mimicking activity of each cycle was measured (Figure S7b). The catalytic activity of the nanozyme remained at over 90 % after seven cycles, with only a slight decrease observed, which may be ascribed to the loss of nanocomposites

during centrifugation. The hypothesis was verified by the result that the XRD of the catalyst after cyclic catalysis did not change significantly compared with the original Co-N-CNTs (Figure S7c, bottom). The catalytic stability was also analyzed in microfluidic chips. It was found that Co-N-CNTs still had good catalytic performance after several hours of continuous circulating operation (Figure 5b). The SEM and TEM were employed to evaluate the physical stability of Co-N-CNTs. As shown in Figure S7d and e, the microstructure of Co-N-CNTs did not change significantly after the catalytic oxidation of TMB and H_2O. According to the above investigations, the Co-N-CNTs nanozyme had excellent structural stability and the long-term durable performance for biocatalysis.

Exploration of catalytic mechanism.

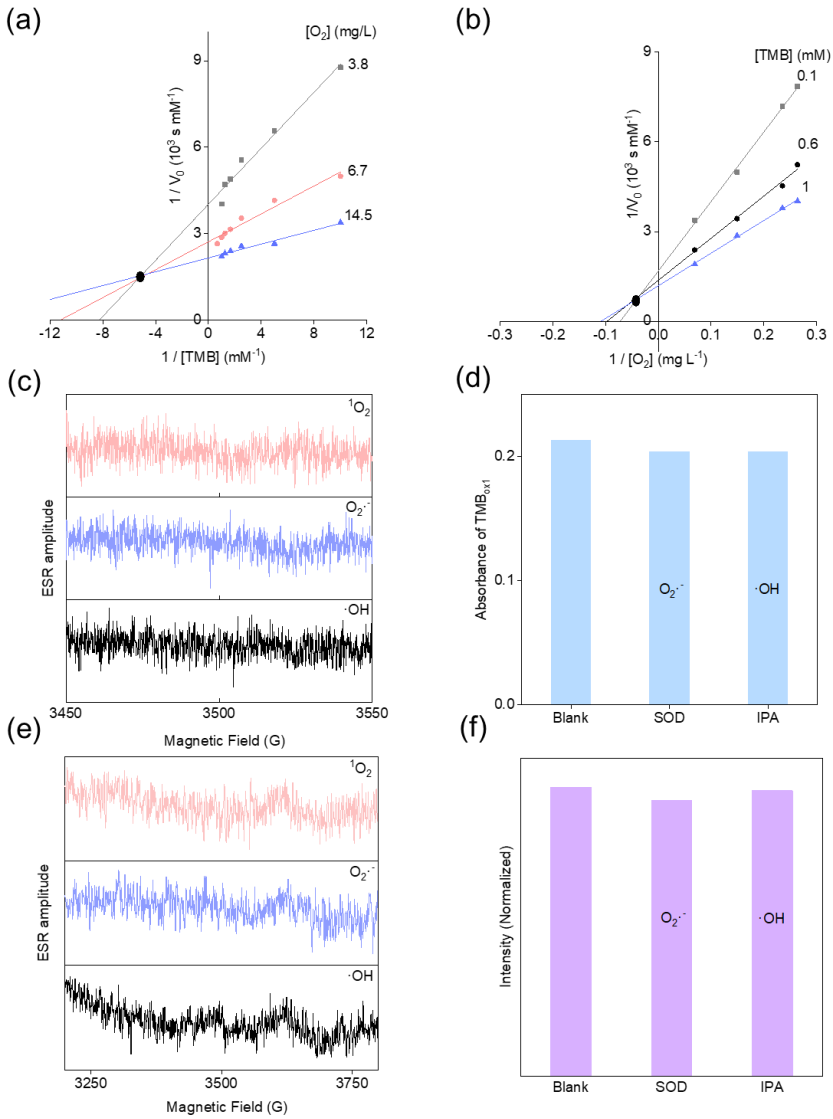

Figure S8. Mechanism studies of oxidase- and catalase-like activity. The Lineweaver–Burk plots for various concentrations of (a) TMB and (b) O_2. Study on the competition between oxidase-like and catalase-like properties. (c) ESR spectra of the spin adduct of the hydroxyl radical, superoxide radical, and singlet oxygen generated during the activation of O_2 by Co-N-CNTs in 0.1 M HAc-NaAc (pH 3.5). (d) The activity changes of oxidation of TMB by Co-N-CNTs after adding SOD (1500 U/ml) and isopropanol (IPA, 0.1 mM) as scavengers to remove the potential superoxide and hydroxyl radicals, respectively. (e) ESR spectra of the spin adduct of the hydroxyl radical, superoxide radical, and singlet oxygen generated during the activation of H_2O_2 by Co-N-CNTs in 0.1 M HAc-NaAc (pH 3.5). (f) The activity changes of decomposition of H_2O_2 by Co-

N-CNTs after adding SOD (1500 U/ml) and isopropanol (IPA, 0.1 mM) as scavengers to remove the potential superoxide and hydroxyl radicals, respectively.

To gain insights of catalase-like activities for Co-N-CNTs, the electron spin resonance (ESR) spectra was carried out to monitor the possible intermediate reactive oxygen species (ROS). It could be seen Figure S8e that there were no signals for any ROS-trapping agent adducts during the expression of catalase-like activity by the Co-N-CNTs nanozyme. Furthermore, SOD and isopropyl alcohol (IPA) were selected as scavengers for monitoring superoxide and hydroxyl radicals. As shown in Figure S8f, the addition of trapping agent also had no significant effect on the decomposition of H_2O_2 by Co-N-CNTs. The results indicated that there was no detectable free radical generation during the catalase-like reaction by the Co-N-CNTs nanozyme.

Nanozymatic reaction networks using Co-N-CNTs.

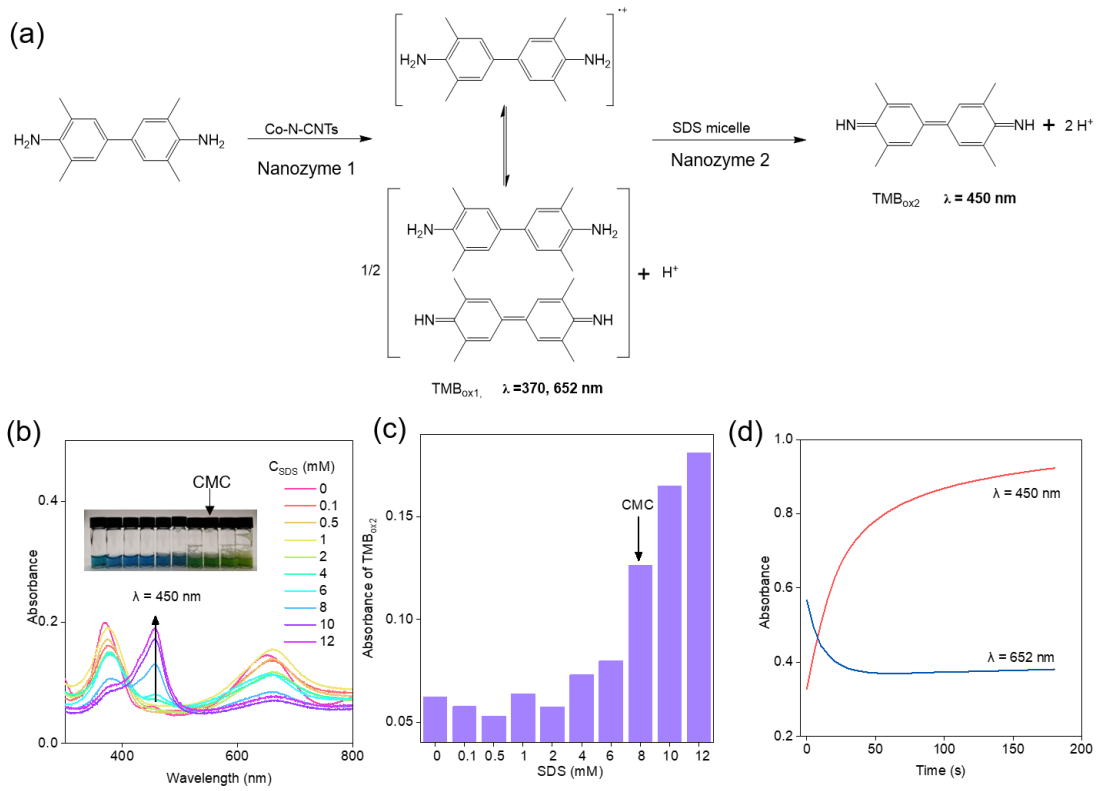

Figure S9. (a) SDS micelle-catalyzed cascade reaction process. (b) UV-vis absorption spectra of the TMB_{ox1} (652 nm) and TMB_{ox2} (450 nm) in the presence of SDS at different concentrations. Inset: The colour changes of P_1 solution with the increase of SDS concentration. (c) Effects of the concentration of SDS on the oxidation of TMB_{ox1} to TMB_{ox2} in P_1 solution. (d) Time-dependent UV-vis absorption of TMB_{ox1} (652 nm) and TMB_{ox2} (450 nm) after SDS (10 mM) was applied to the P_1 solution.

To confirm the role of SDS micelles on the catalysis process, the influence of different concentrations of SDS on catalytic reaction was studied. As shown in Figures S9b and c, when the concentration of SDS was much less than critical micelle concentration (CMC), the surfactant exhibited no obvious catalytic effect on the oxidation of TMB_{ox1}. However, when the critical micelle concentration (ca. ≥ 8 mM) reached, a catalytic effect was prominently observed, making TMB_{ox1} further be oxidized to TMB_{ox2}, indicating that the catalytic effect was attributable to micelle formation. In order to eliminate the stimulus of continuous oxidation by Co-N-CNTs, the catalyst was removed from the reaction solution. The filtrated supernatant was

denoted as P_1. The change of substance concentration in the reaction system after adding SDS micelles was monitored by time-dependent UV-vis spectroscopy. It was found that the absorbance of TMB_{ox2} (450 nm) increased in a few seconds, accompanied by a decrease in TMB_{ox1} (652 nm, Figure S9d). It suggested that this cascade reaction was successfully constructed by Co-N-CNTs (E_1) and SDS micelles (E_2).

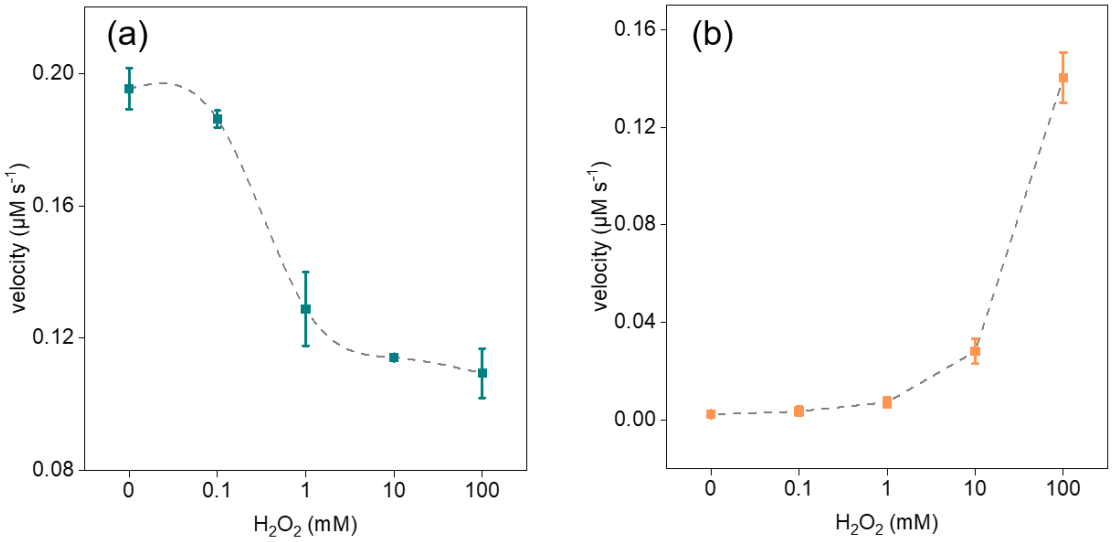

Figure S10. Diverse response of the chemical reaction network caused by a single stimulation using H_2O_2**.**

Nanozymatic network-based cell mimics enabling highly selective and wide-range linear response to H_2O_2

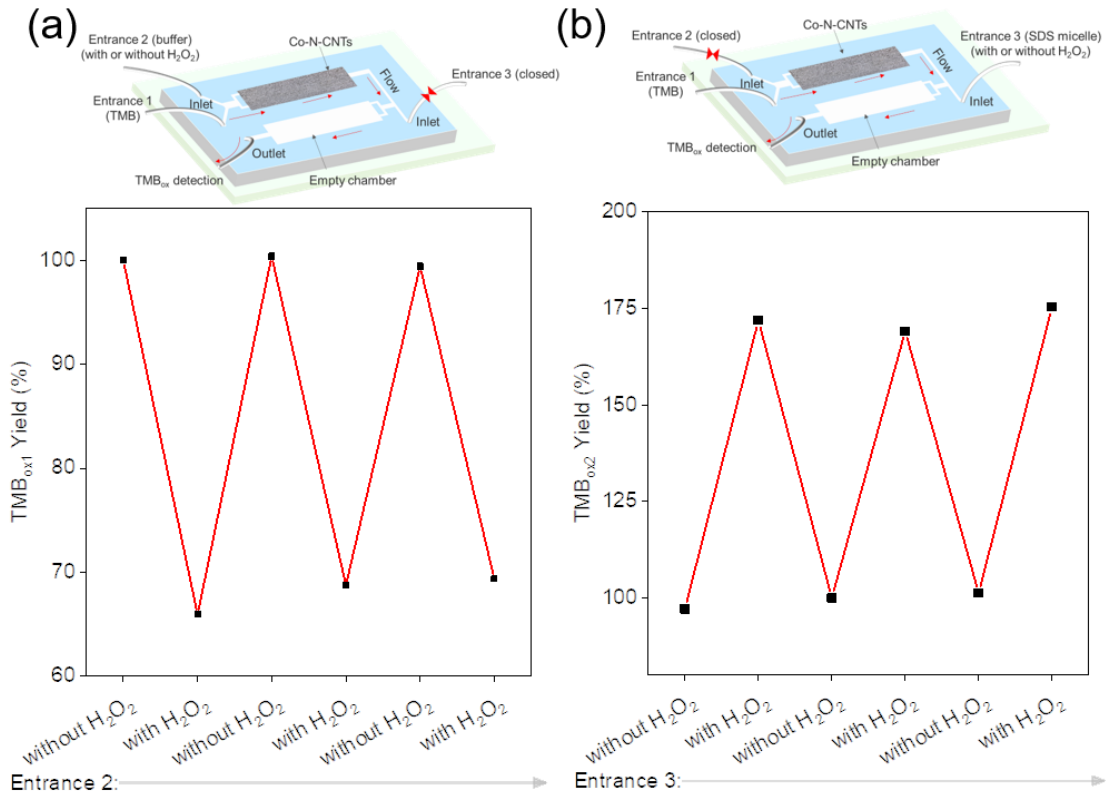

Figure S11. Regulatory mode cycles in microfluidics. (a) Feedback, (b) Feedforward. Top panel: Configuration of the microfluidic device.

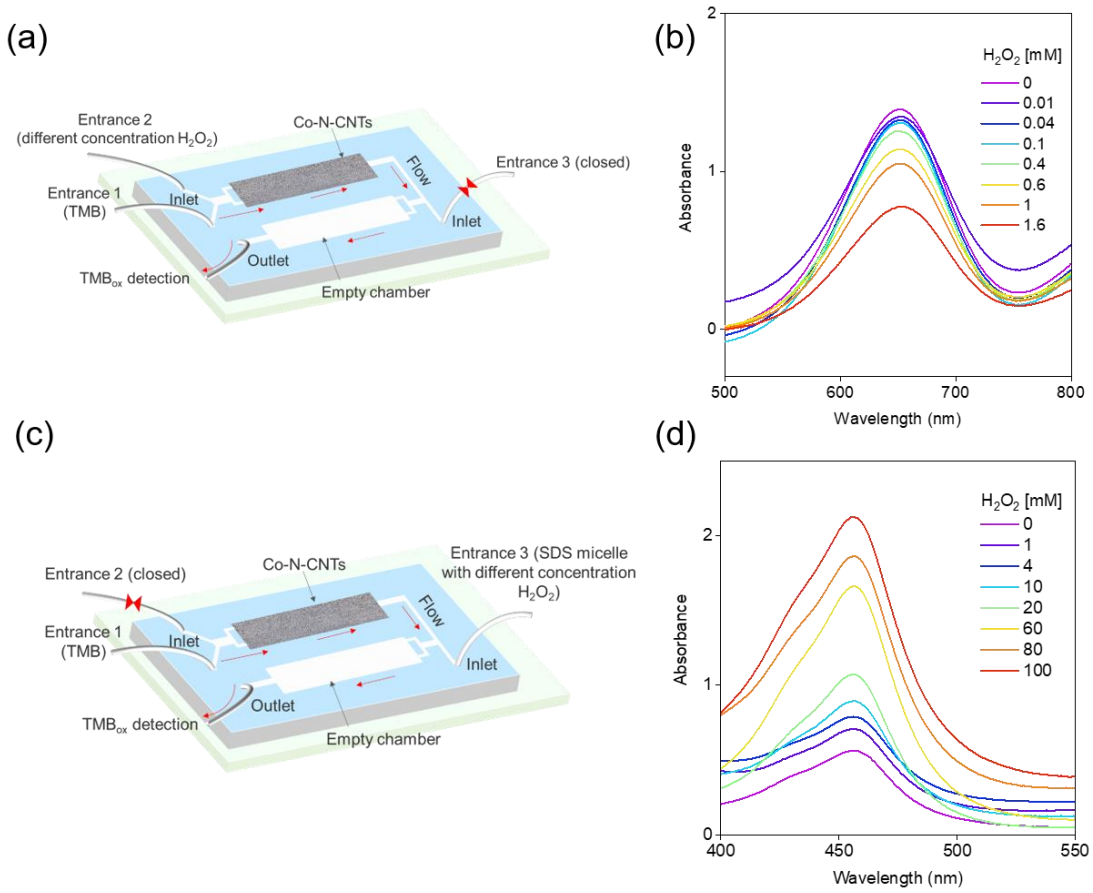

Figure S12. Configuration of the microfluidic device for feedback (a) and feedforward (c). UV-vis absorption spectra of TMB after response to H_2O_2 in the (b) feedback and (d) feedforward responsiveness.

Table S4. Comparison of colorimetric method in response to H_2O_2 using different materials in the literatures.

Methods	materials	Linear range	Ref.
Colorimetry	Co_3O_4@β-CDNPs	0.3-3.0 μM	[23]
Colorimetry	FeS nanosheets	5-150 μM	[24]
Colorimetry	$Co_{0.5}Ni_{0.5}Fe_2O_4$ nanoparticles	0.5-20 μM	[25]
Colorimetry	Pd-LNT NPs	3-107 μM	[26]
Colorimetry	NS-CQDs	0.02-0.1 mM	[27]
Colorimetry	nanozymatic network	10-1600 μM 1-100 mM	This work

Notably, to date, many techniques can be quantitatively responsive to H_2O_2, including the electrochemical, fluorescence, and colorimetric methods.[28-30] Among them, colorimetric techniques are easier to implement in practical applications,[31-32] but suffer from narrow response range.[30, 33] This was due to the fact that colorimetry is usually achieved by catalytic reactions. However, at high hydrogen peroxide concentrations, nearly all catalysts are inactivated by a pathway called "suicide-peroxide inactivation".[34-35] Therefore, although many works in detecting ultra-low concentration of H_2O_2 have been reported, the highly selective and linear response to H_2O_2 at high concentrations in a variety of practical environments is a challenge. Thanks to the multiple response of variable intensities for the network to stimulus, the colorimetric response to H_2O_2 in concentration from micromoles to tens of millimoles per liter was realized. Compared with previous works quantitatively responsive to H_2O_2 (Table S4), the proposed cell mimics demonstrated a wider range of linear response range.

References

1. Ji, S.; Jiang, B.; Hao, H.; Chen, Y.; Dong, J.; Mao, Y.; Zhang, Z.; Gao, R.; Chen, W.; Zhang, R.; Liang, Q.; Li, H.; Liu, S.; Wang, Y.; Zhang, Q.; Gu, L.; Duan, D.; Liang, M.; Wang, D.; Yan, X.; Li, Y., Matching the kinetics of natural enzymes with a single-atom iron nanozyme. *Nat. Catal.* **2021,** *4*, 407-417.

2. Grimme, S.; Ehrlich, S.; Goerigk, L., Effect of the damping function in dispersion corrected density functional theory. *J. Comput. Chem.* **2011,** *32*, 1456-1465.

3. Grimme, S.; Antony, J.; Ehrlich, S.; Krieg, H., A consistent and accurate ab initio parametrization of density functional dispersion correction (DFT-D) for the 94 elements H-Pu. *J. Chem. Phys.* **2010,** *132*, 154104.

4. Perdew, J. P.; Burke, K.; Ernzerhof, M., Generalized gradient approximation made simple. *Phys. Rev. Lett.* **1996,** *77*, 3865.

5. Xu, H.; Cheng, D.; Cao, D.; Zeng, X. C., A universal principle for a rational design of single-atom electrocatalysts. *Nat. Catal.* **2018,** *1*, 339-348.

6. Monkhorst, H. J.; Pack, J. D., Special points for Brillouin-zone integrations. *Phys. Rev. B* **1976,** *13*, 5188.

7. Kresse, G.; Furthmüller, J., Efficiency of ab-initio total energy calculations for metals and semiconductors using a plane-wave basis set. *Comput. Mater. Sci.* **1996,** *6*, 15-50.

8. Kresse, G.; Joubert, D., From ultrasoft pseudopotentials to the projector augmented-wave method. *Phys. Rev. B* **1999,** *59*, 1758.

9. Blöchl, P. E., Projector augmented-wave method. *Phys. Rev. B* **1994,** *50*, 17953.

10. Andreiadis, E. S.; Jacques, P. A.; Tran, P. D.; Leyris, A.; Chavarot-Kerlidou, M.; Jousselme, B.; Matheron, M.; Pecaut, J.; Palacin, S.; Fontecave, M.; Artero, V., Molecular engineering of a cobalt-based electrocatalytic nanomaterial for H_2 evolution under fully aqueous conditions. *Nat. Chem.* **2013,** *5*, 48-53.

11. Pan, Y.; Lin, R.; Chen, Y.; Liu, S.; Zhu, W.; Cao, X.; Chen, W.; Wu, K.; Cheong, W. C.; Wang, Y.; Zheng, L.; Luo, J.; Lin, Y.; Liu, Y.; Liu, C.; Li, J.; Lu, Q.; Chen, X.;

Wang, D.; Peng, Q.; Chen, C.; Li, Y., Design of Single-Atom Co-N_5 Catalytic Site: A Robust Electrocatalyst for CO_2 Reduction with Nearly 100% CO Selectivity and Remarkable Stability. *J. Am. Chem. Soc.* **2018,** *140*, 4218-4221.

12. Ding, W.; Wei, Z.; Chen, S.; Qi, X.; Yang, T.; Hu, J.; Wang, D.; Wan, L.; Alvi, S. F.; Li, L., Space-confinement-induced synthesis of pyridinic- and pyrrolic-nitrogen-doped graphene for the catalysis of oxygen reduction. *Angew. Chem., Int. Ed.* **2013,** *52*, 11755-11759.

13. Sa, Y. J.; Park, C.; Jeong, H. Y.; Park, S. H.; Lee, Z.; Kim, K. T.; Park, G. G.; Joo, S. H., Carbon nanotubes/heteroatom-doped carbon core-sheath nanostructures as highly active, metal-free oxygen reduction electrocatalysts for alkaline fuel cells. *Angew. Chem., Int. Ed.* **2014,** *53*, 4102-4106.

14. Josephy, P. D.; Eling, T.; Mason, R. P., The horseradish peroxidase-catalyzed oxidation of 3,5,3',5'-tetramethylbenzidine. Free radical and charge-transfer complex intermediates. *J. Biol. Chem.* **1982,** *257*, 3669-3675.

15. Xu, Y.; Xue, J.; Zhou, Q.; Zheng, Y.; Chen, X.; Liu, S.; Shen, Y.; Zhang, Y., The Fe-N-C Nanozyme with Both Accelerated and Inhibited Biocatalytic Activities Capable of Accessing Drug-Drug Interactions. *Angew. Chem., Int. Ed.* **2020,** *59*, 14498-14503.

16. Bhattacharyya, S.; Ali, S. R.; Venkateswarulu, M.; Howlader, P.; Zangrando, E.; De, M.; Mukherjee, P. S., Self-Assembled Pd_{12} Coordination Cage as Photoregulated Oxidase-Like Nanozyme. *J. Am. Chem. Soc.* **2020,** *142*, 18981-18989.

17. Wu, Y.; Jiao, L.; Luo, X.; Xu, W.; Wei, X.; Wang, H.; Yan, H.; Gu, W.; Xu, B. Z.; Du, D., Oxidase-Like Fe-N-C single-atom nanozymes for the detection of acetylcholinesterase activity. *Small* **2019,** *15*, 1903108.

18. Wu, R.; Sun, M.; Liu, X.; Qin, F.; Zhang, X.; Qian, Z.; Huang, J.; Li, Y.; Tan, T.; Chen, W.; Chen, Z., Oxidase-like ZnCoFe Three-Atom Nanozyme as a Colorimetric Platform for Ascorbic Acid Sensing. *Anal. Chem.* **2022,** *94*, 14308-14316.

19. Zhang, R.; Xue, B.; Tao, Y.; Zhao, H.; Zhang, Z.; Wang, X.; Zhou, X.; Jiang, B.; Yang, Z.; Yan, X., Edge-Site Engineering of Defective Fe–N_4 Nanozymes with Boosted Catalase-Like Performance for Retinal Vasculopathies. *Adv. Mater.* **2022,** *34*,

2205324.

20. Fan, J.; Yin, J.-J.; Ning, B.; Wu, X.; Hu, Y.; Ferrari, M.; Anderson, G. J.; Wei, J.; Zhao, Y.; Nie, G., Direct evidence for catalase and peroxidase activities of ferritin–platinum nanoparticles. *Biomaterials* **2011,** *32*, 1611-1618.

21. Wang, F.; Ju, E.; Guan, Y.; Ren, J.; Qu, X., Light-Mediated Reversible Modulation of ROS Level in Living Cells by Using an Activity-Controllable Nanozyme. *Small* **2017,** *13*, 1603051.

22. Mu, X.; He, H.; Wang, J.; Long, W.; Li, Q.; Liu, H.; Gao, Y.; Ouyang, L.; Ren, Q.; Sun, S., Carbogenic nanozyme with ultrahigh reactive nitrogen species selectivity for traumatic brain injury. *Nano Lett.* **2019,** *19*, 4527-4534.

23. Han, D.-M.; Matthew Zhang, Q.; Serpe, M. J., Poly (N-isopropylacrylamide)-co-(acrylic acid) microgel/Ag nanoparticle hybrids for the colorimetric sensing of H_2O_2. *Nanoscale* **2015,** *7*, 2784-2789.

24. Duan, Y.; Li, Q.; He, P.; Li, Y.; Song, J.; Wang, J.; Liu, J.; Zhou, J.; Chen, F.; Huang, Z.; Sun, J.; Zhang, Y.; Luo, Z., Ultrathin FeS nanosheets with high chemodynamic activity for sensitive colorimetric detection of H_2O_2 and glutathione. *Chin. Chem. Lett.* **2022,** *33*, 3217-3220.

25. Zhu, X.; Li, H.; Wu, T.; Zhao, H.; Wu, K.; Xu, W.; Qin, F.; Chen, W.; Zheng, J.; Liu, Q., In situ decorating the surface and interlayer of montmorillonite with $Co_{0.5}Ni_{0.5}Fe_2O_4$ nanoparticles: A sustainable, biocompatible colorimetric platform for H_2O_2 and acetylcholine. *Nano Res.* **2022,** *15*, 9319-9326.

26. Li, R.; Dong, L.; Liang, Y.; Cui, Y.; Ji, X.; Xiao, H.; Gao, S.; Wang, L., Palladium Nanoparticles Stabilized by Lentinan with Enhanced Peroxidase-like Activity for Sensitive Detection of H_2O_2. *ChemistrySelect* **2022,** *7*.

27. Singh, V. K.; Yadav, P. K.; Chandra, S.; Bano, D.; Talat, M.; Hasan, S. H., Peroxidase mimetic activity of fluorescent NS-carbon quantum dots and their application in colorimetric detection of H_2O_2 and glutathione in human blood serum. *J. Mater. Chem. B* **2018,** *6*, 5256-5268.

28. Fang, K.; Yang, Y.; Fu, L.; Zheng, H.; Yuan, J.; Niu, L., Highly selective H_2O_2 sensor based on 1-D nanoporous Pt@C hybrids with core-shell structure. *Sens.*

Actuators, B **2014,** *191*, 401-407.

29. Wang, M.; Zhang, F.; Wang, C. Q.; Yin, N.; Wang, Y.; Qin, G.; Xu, Q.; Gong, J.; Liu, H.; Duan, X., Target-Binding Accelerated Response for Sensitive Detection of Basal H_2O_2 in Tumor Cells and Tissues via a Dual-Functional Fluorescence Probe. *Anal. Chem.* **2022,** *94*, 5962-5969.

30. Ma, C. B.; Xu, Y.; Wu, L.; Wang, Q.; Zheng, J.; Ren, G.; Wang, X.; Gao, X.; Zhou, M.; Wang, M.; Wei, H., Guided Synthesis of a Mo/Zn Dual Single-Atom Nanozyme with Synergistic Effect and Peroxidase-like Activity. *Angew. Chem. Int. Ed.* **2022,** *61*, e202116170.

31. Li, Q.; Ren, S.; Peng, Y.; Lv, Y.; Wang, W.; Wang, Z.; Gao, Z., A Colorimetric Strip for Rapid Detection and Real-Time Monitoring of Histamine in Fish Based on Self-Assembled Polydiacetylene Vesicles. *Anal. Chem.* **2019,** *92*, 1611-1617.

32. Wang, G.; Huang, S.; He, H.; Cheng, J.; Zhang, T.; Fu, Z.; Zhang, S.; Zhou, Y.; Li, H.; Liu, X., Fabrication of a "progress bar" colorimetric strip sensor array by dye-mixing method as a potential food freshness indicator. *Food Chem.* **2022,** *373*, 131434.

33. Cheng, X.; Huang, L.; Yang, X.; Elzatahry, A. A.; Alghamdi, A.; Deng, Y., Rational design of a stable peroxidase mimic for colorimetric detection of H_2O_2 and glucose: A synergistic CeO_2/Zeolite Y nanocomposite. *J. Colloid Interface Sci.* **2019,** *535*, 425-435.

34. Valderrama, B.; Ayala, M.; Vazquez-Duhalt, R., Suicide inactivation of peroxidases and the challenge of engineering more robust enzymes. *Chem. Biol.* **2002,** *9*, 555-565.

35. Song, Y.; Qu, K.; Zhao, C.; Ren, J.; Qu, X., Graphene Oxide: Intrinsic Peroxidase Catalytic Activity and Its Application to Glucose Detection. *Adv. Mater.* **2010,** *22*, 2206-2210.